Monthly Notices of the ROYAL ASTRONOMICAL SOCIETY

MNRAS **508,** 5854–5863 (2021) https://doi.org/10.1093/mnras/stab2873
Advance Access publication 2021 October 7

Presence of red giant population in the foreground stellar substructure of the Small Magellanic Cloud

Dizna James,[1]★ Smitha Subramanian,[2]★ Abinaya O. Omkumar,[2,3,4] Adhya Mary,[1] Kenji Bekki,[5] Maria-Rosa L. Cioni,[3] Richard de Grijs,[6,7] Dalal El Youssoufi,[3,4] Sreeja S. Kartha,[1] Florian Niederhofer[3] and Jacco Th. van Loon[8]

[1]*Department of Physics, Christ (Deemed to be) University, Bangalore, 560029, India*
[2]*Indian Institute of Astrophysics, Koramangala II Block, Bangalore, 560034, India*
[3]*Leibniz-Institut für Astrophysik Potsdam (AIP), An der Sternwarte 16, D-14482 Potsdam, Germany*
[4]*Institut für Physik und Astronomie, Universität Potsdam, Haus 28, Karl Liebknecht Str 24/25, D-14476 Golm (Potsdam), Germany*
[5]*ICRAR, M468, The University of Western Australia, 35 Stirling Highway, Crawley, WA 6009, Australia*
[6]*Department of Physics and Astronomy, Macquarie University, Balaclava Road, Sydney, NSW 2109, Australia*
[7]*Research Centre for Astronomy, Astrophysics and Astrophotonics, Macquarie University, Balaclava Road, Sydney, NSW 2109, Australia*
[8]*Lennard-Jones Laboratories, Keele University, Keele ST5 5BG, UK*

Accepted 2021 September 23. Received 2021 September 22; in original form 2021 July 24

ABSTRACT

The eastern region of the Small Magellanic Cloud (SMC) is found to have a foreground stellar substructure, which is identified as a distance bimodality (∼12 kpc apart) in the previous studies using red clump (RC) stars. Interestingly, studies of red giant branch (RGB) stars in the eastern SMC indicate a bimodal radial velocity (RV) distribution. In this study, we investigate the connection between these two bimodal distributions to better understand the nature and origin of the foreground stellar substructure in the eastern SMC. We use the *Gaia* Early Data Release 3 astrometric data and archival RV data of RGB stars for this study. We find a bimodal RV distribution of RGB stars (separated by ∼35–45 km s^{-1}) in the eastern and south-western (SW) outer regions. The observed proper motion values of the lower and higher RV RGB components in the eastern regions are similar to those of the foreground and main-body RC stars, respectively. This suggests that the two RGB populations in the eastern region are separated by a similar distance to those of the RC stars, and the RGB stars in the lower RV component are part of the foreground substructure. Based on the differences in the distance and RV of the two components, we estimate an approximate time of formation of this substructure as 307 ± 65 Myr ago. This is comparable with the values predicted by simulations for the recent epoch of tidal interaction between the Magellanic Clouds. Comparison of the observed properties of RGB stars, in the outer SW region, with *N*-body simulations shows that the higher RV component in the SW region is at a farther distance than the main body, indicating the presence of a stellar counter-bridge in the SW region of the SMC.

Key words: proper motions – stars: kinematics and dynamics – galaxies: individual: Small Magellanic Cloud – galaxies: interactions – Magellanic Clouds.

1 INTRODUCTION

According to the Lambda cold dark matter model, galaxies grow in mass through the hierarchical assembly of smaller systems (Fall & Efstathiou 1980; van den Bosch 2002; Agertz, Teyssier & Moore 2011). Thus, interactions and mergers play a significant role in the evolution of galaxies. One of the nearest examples of an ongoing hierarchical merging process is the Large Magellanic Cloud (LMC)–Small Magellanic Cloud (SMC) galaxy pair, interacting mutually and with the Milky Way. The LMC and the SMC are two gas-rich interacting dwarf galaxies located at a distance of 50 ± 2 kpc (LMC; de Grijs, Wicker & Bono 2014) and 62 ± 1 kpc (SMC; de Grijs & Bono 2015), respectively. There exists a bridge of gas and stars connecting these galaxies known as the Magellanic Bridge (MB), a leading and a trailing stream of gas known as the Leading Arm (LA) and the Magellanic Stream (MS), respectively. The MB, MS, and LA are prominent features in H I maps (Putman et al. 2003).

Simulations of the Magellanic System (Besla et al. 2012; Diaz & Bekki 2012), based on revised proper motion estimates of the Magellanic Clouds (MCs) (Kallivayalil et al. 2006; Vieira et al. 2010), explain the formation of the observed gaseous features around the MCs as a result of their mutual interactions. The dominant nature of these interactions is suggested to be tidal, predicting the presence of stellar substructures along with the gaseous features around the MCs. According to these simulations, the MS and the MB were formed ∼1.5 Gyr and ∼100–300 Myr ago, respectively, mainly from material stripped from the SMC. However, the MS has also been suggested to contain material stripped from the LMC (Nidever,

★ E-mail: diznajames28@gmail.com (DJ); smitha.subramanian@iiap.res.in (SS)

Majewski & Butler Burton 2008; Hammer et al. 2015; Richter et al. 2017), and based on the observed low metal abundance of stars in the MB, Ramachandran, Oskinova & Hamann (2021) suggested that the time of the initial formation of the MB may date back to several billion years. Based on the relative motions of the MCs and recent proper motion measurements of stars within the MB region (Gaia Collaboration 2016, 2018), the tidal interaction event that formed the MB is suggested to have happened ∼150 Myr ago (Zivick et al. 2018, 2019; Schmidt et al. 2019). Although tidal interactions must have played a dominant role, ram-pressure effects due to the Milky Way's halo could have also altered the present shape of the gaseous features of the Magellanic System (Hammer et al. 2015; Salem et al. 2015; Tepper-García et al. 2019; Wang et al. 2019).

Stellar substructures formed during the formation of the MB and MS are expected to contain stars older than ∼300 Myr and ∼1.5 Gyr, respectively. Although several studies (Nidever et al. 2011; Bagheri, Cioni & Napiwotzki 2013; Noël et al. 2013, 2015; Skowron et al. 2014; Belokurov et al. 2017; Jacyszyn-Dobrzeniecka et al. 2017, 2020; Massana et al. 2020) found intermediate-age/old (age >2 Gyr) stars around the MB region, the interpretations of their origin differed. While Noël et al. (2013, 2015) and Carrera et al. (2017) supported a tidal origin for these intermediate-age stars, Jacyszyn-Dobrzeniecka et al. (2017) and Wagner-Kaiser & Sarajedini (2017) suggested that they were part of the overlapping stellar haloes of the MCs. No conclusive evidence of a stellar counterpart (consisting of stars older than 1.5 Gyr) to the MS has been found so far. However, the MB and LA host stellar populations of a few Myr (Demers & Battinelli 1998; Harris 2007; Chen et al. 2014; Skowron et al. 2014; Nidever et al. 2019; Price-Whelan et al. 2019 and references therein), which might have formed from the gas stripped during the interactions of the MCs.

Nidever et al. (2013) identified a foreground population (∼10–12 kpc in front of the SMC main body) of red clump (RC) stars (which are standard candles) in four distinct 0.36 deg^2 fields at a radius of 4° from the SMC centre to the east (in the direction of the MB and the LMC). Subramanian et al. (2017) and Tatton et al. (2020) studied this feature using a subset and a complete set of near-infrared data of RC stars, obtained from the *VISTA* (Visible and Infrared Survey Telescope for Astronomy) survey of the MCs (VMC; Cioni et al. 2011), respectively. VMC data being continuous and homogeneous allowed both these studies to trace this foreground RC feature over 2.5–4° from the SMC centre to the east. All these studies suggested that this foreground RC population could be the result of interactions between the MCs. Nidever et al. (2013) and Subramanian et al. (2017) suggested a tidal origin for this feature, a tidally stripped stellar population from the SMC during the interaction between the MCs around 300 Myr ago, which in turn might have caused the formation of the MB. However, Tatton et al. (2020) added that as some of these substructures are traced only by RC stars and not by RR Lyrae stars, tidal effects cannot fully explain this RC feature and ram-pressure effects might also be involved. Nidever et al. (2013), Subramanian et al. (2017), and Tatton et al. (2020) could not probe this feature beyond 4° from the SMC centre, due to the limited spatial coverage of the data.

Omkumar et al. (2021) analysed this dual RC feature using *Gaia* Data Release 2 (DR2; Gaia Collaboration 2018) data of an ∼314 deg^2 region centred on the SMC, which cover the entire SMC and a significant portion of the MB. They found that the *Gaia* DR2 data trace this foreground RC feature from ∼2.5° to 5–6° from the optical centre of the SMC in the eastern regions towards the MB and that it does not fully overlap with the MB in the plane of the sky. However, El Youssoufi et al. (2021) detected this feature out to a 10° distance from the SMC centre, in the direction of the MB. They used the near infrared (NIR) data from VISTA Hemisphere Survey (VHS; McMahon et al. 2017). Omkumar et al. (2021) found that the proper motion values of the bright (foreground) RC were found to be significantly larger than those of the faint (main-body) RC, which is expected if the bright RC is at a closer distance. The authors found that the foreground stellar population is kinematically distinct from the stellar population of the main body with ∼35 km s^{-1} slower tangential velocity and moving to the north-west relative to the main body. They found that although the observed properties of this foreground RC feature are not completely consistent with those predicted by the simulations of Diaz & Bekki (2012), a comparison indicated that the foreground stellar substructure is most likely a tidally stripped counterpart of the gaseous MB and might have formed from the inner disc (dominated by stars) of the SMC.

A foreground stellar substructure formed due to the tidal interactions of the MCs is expected to have all types of stars older than the epoch of interaction, which presumably formed this substructure. So, if the foreground RC feature is formed due to tidal effects operating during the formation of the MB, ∼100–300 Myr ago, then we expect SMC stars older than 300 Myr to have a line-of-sight distance distribution similar to what is observed for RC stars. In a study of RR Lyrae stars (older than 10 Gyr) in the SMC using VMC data, Muraveva et al. (2018) did not find a clear distance bimodality in the 2.5–4° eastern regions (especially in the north-eastern regions) as observed in the RC distribution. However, as suggested by Omkumar et al. (2021), if the foreground RC population is tidally stripped from the disc of the SMC and the RR Lyrae stars are located in the less disturbed spheroidal component, then the observed difference in the line-of-sight distance distribution of RC stars and RR Lyrae stars in the SMC can be explained.

Another numerous and homogeneously distributed intermediate-age/old stellar tracer in a galaxy is red giant branch (RGB) stars. The dominant population of the RGB stars in the SMC has an age of ∼5 Gyr (Rubele et al. 2018; El Youssoufi 2019). As RGB stars are not standard candles, it is not trivial to obtain their line-of-sight distance distribution. However, the tip of the RGB is a well-known standard candle and is used to estimate the distance to nearby galaxies. Groenewegen et al. (2019) estimated the distance to different regions of the SMC in the VMC footprint and the results indicated a shorter distance in the eastern regions. A spectroscopic study of RGB stars in the central 4° region of the SMC by Dobbie et al. (2014) identified a bimodality in their radial velocity distribution in the eastern SMC, the regions where the RC distance bimodality is observed. They suggested that the bimodal radial velocity distribution could be due to the tidal interaction between the MCs. It will be interesting to infer the distances to these RGB stars with bimodal radial velocity distribution and compare with the distance of the foreground RC feature. Due to the difficulty in estimating the distances to these RGB stars, another way is to check the proper motion values of the RGB stars in the two components of the radial velocity distribution and compare them with the observed proper motion values of the foreground and main-body RC stars by Omkumar et al. (2021). If the RGB stars in the two radial velocity components are located at two different distances along the line of sight (similar to the foreground and the main-body RC stars), then their relative proper motion value is expected to match that of the relative proper motion between the foreground and main-body RC stars. In this context, we combine the radial velocity data from Dobbie et al. (2014) and De Leo et al. (2020) with the proper motion data from the Early Data Release 3 (EDR3) of *Gaia* to obtain 3D kinematic information of RGB stars in the central 4.5° radial region of the SMC and to understand the effect

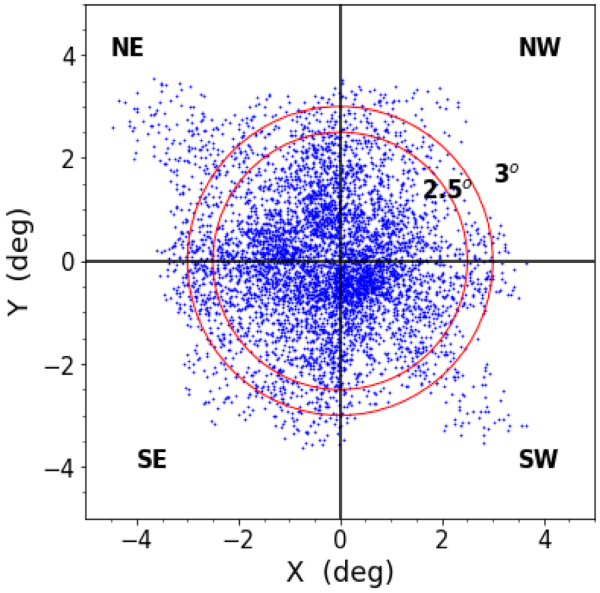

Figure 1. Cartesian plot showing the distribution of RGB sources (blue) analysed in this study. The red circle encompasses the 2.5° and 3° radial region around the SMC from its optical centre (de Vaucouleurs & Freeman 1972) and the divisions of sectors are marked with the black lines.

of tidal interaction on another intermediate-age stellar tracer in the SMC.

The structure of this paper is as follows. Data used in the study are described in Section 2. The analysis and results are presented in Section 3. Section 4 provides a summary.

2 DATA

We use the radial velocity data of 4172 RGB stars in the SMC provided by Dobbie et al. (2014) and 1861 RGB stars by De Leo et al. (2020). The two data sets are consistent with each other and the typical difference in the measurements of common stars (175 stars) in the two data sets is $\sim$1 km s^{-1}. The sample is distributed in an area of $\sim$37.5 deg^2 of the central SMC. The optical spectra of these RGB stars were obtained with the multiobject optical spectrograph 2dF/AAOmega instrument on the 3.9 m *Anglo-Australian Telescope* at *Siding Spring Observatory*, Australia. The proper motion data were taken from *Gaia* EDR3 (Gaia Collaboration 2020). Out of 5859 sources (after removing duplicate sources) with radial velocity data, we could extract the proper motion values for 5750 sources (which are matched within 1 arcsec). Stars with no proper motion measurements in the RA, μ_α, and Dec, μ_δ, directions are removed from our further analysis. Moreover, we applied a cut to the proper motion values based on the expected range in their values (-3 mas yr^{-1} $\leq \mu_\alpha \leq$ $+3$ mas yr^{-1} and -3 mas yr^{-1} $\leq \mu_\delta \leq +3$ mas yr^{-1}) predicted by simulations (Diaz & Bekki 2012) for the SMC main-body and stellar tidal features around the SMC. This cut reduces the number of stars for further analysis to 5664.

2.1 Division of subregions

Fig. 1 shows the spatial distribution of the RGB stars analysed in this study. The Cartesian plot (zenithal equidistant projection) is obtained by converting the RA and Dec of the RGB sources into X and Y, respectively, using the equations provided by van der Marel & Cioni (2001) and considering the optical centre of the SMC $\alpha_S = 00^h52^m12\overset{s}{.}5$ and $\delta_S = -72°49'43''$ (de Vaucouleurs & Freeman 1972) as the origin. Initially the sources were divided into four sectors, namely north-east (NE; $Y > 0$ and $X < 0$), north-west (NW; $Y > 0$ and $X > 0$), south-east (SE; $Y < 0$ and $X < 0$), and south-west (SW; $Y < 0$ and $X > 0$). Previous studies using the RC stars (Subramanian et al. 2017; Omkumar et al. 2021) traced the foreground RC feature beyond 2$\overset{\circ}{.}$5 in the eastern regions of the SMC. Therefore, each sector is further subdivided into inner ($R \leq 2\overset{\circ}{.}5$) and outer ($R > 2\overset{\circ}{.}5$) subregions. The red circles in Fig. 1 mark the 2$\overset{\circ}{.}$5 and 3° radial regions centred on the optical centre of the SMC, and the sector-wise division is shown using the black lines across the spatial distribution of the RGB sources.

3 ANALYSIS AND RESULTS

In this study, we analyse the radial velocities and proper motions of the selected RGB stars. We compare the results from the RGB stars with the proper motion values of the RC stars. We also compare our results with simulations of the SMC (Diaz & Bekki 2012).

3.1 Radial velocity distribution of RGB stars

The radial velocity distributions of each of the subregions are obtained. The majority of the stars have radial velocity values between 100 and 200 km s^{-1}. The average uncertainty in the radial velocities is less than 5 km s^{-1}. The number of stars in different subregions (described in Section 2.1) ranges from 148 to 1451. Based on the number of stars in different subregions and the radial velocity range, we selected an optimal bin size of 10 km s^{-1} [to have number of bins $\leq$ (number of stars in each subregion)$^{0.5}$] to obtain the radial velocity distribution of stars in subregions. Fig. 2 shows the radial velocity distribution of subregions and the panels are arranged according to the spatial distribution of the RGB stars (Fig. 1) on the sky. The outer regions ($R > 2\overset{\circ}{.}5$) are relatively less populated compared with the inner regions. The outer NE ($R > 2\overset{\circ}{.}5$) and SE ($R > 2\overset{\circ}{.}5$) sectors show clear bimodality (top left-hand and bottom left-hand panels of Fig. 2). The observed radial velocity distributions are fitted with Gaussian functions to find the peak velocities. The observed distributions are initially fitted using a single Gaussian function. An additional Gaussian is added if the reduced χ^2 of the fit improves by 30 per cent or more, compared to the reduced χ^2 value of a single Gaussian fit and the full width at half maximum (FWHM) of the second Gaussian component is larger than the bin size of the distribution. We use the PYTHON program CURVE-FIT for the fitting procedure. The subregions with their best-fitting profiles are shown in Fig. 3. The best-fitting parameters along with their errors and χ^2 values are provided in Table 1.

The observed radial velocity distribution of RGB stars in all inner regions and the NW outer region are well fitted with a single Gaussian component (Fig. 3). We can see that the observed radial distributions of the outer NE and SE regions require two Gaussian components. The individual Gaussian components, the lower and higher velocity components (blue and green, respectively), and the combined fit (red) are shown. This suggests a dual population of RGB stars in the NE and SE with $R > 2\overset{\circ}{.}5$. Although there are two components, they overlap significantly. The difference between the peaks of the two components is less than the sum of the widths of the two distributions. Since the components are not well separated, it is difficult to identify/select the probable members of each component. Hence, we selected the inner and outer subregions in the NE and SE using the $R \leq 3°$ and $R > 3°$ criterion, respectively. The radial velocity distributions showed clear bimodality in the outer subregions. The

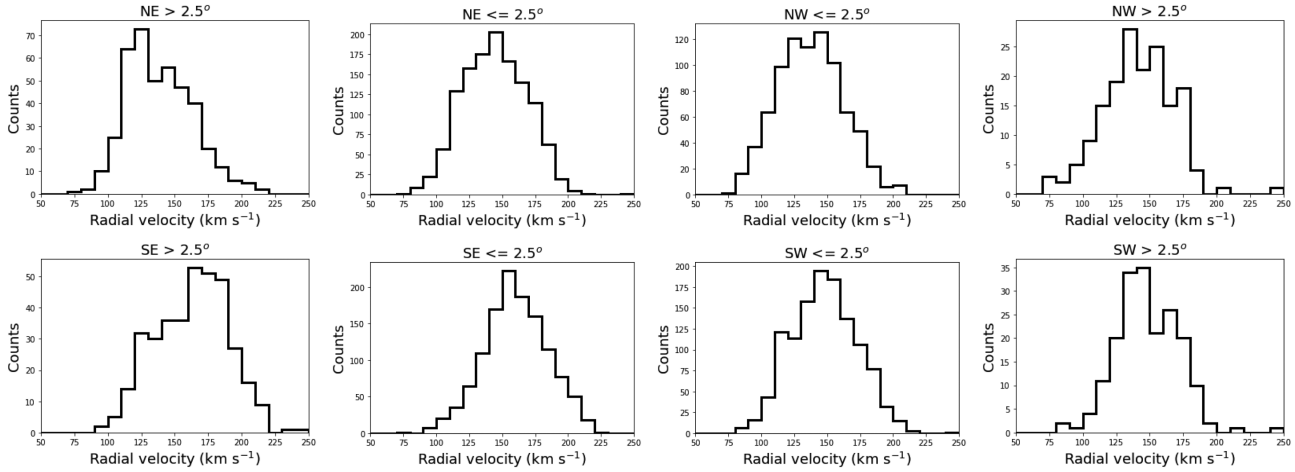

Figure 2. Radial velocity distributions of northern and southern subregions are shown in the first and second rows, respectively. The first two panels in both rows represent eastern (outer: $R > 2.^{\circ}5$; inner: $R \leq 2.^{\circ}5$) subregions and the next two correspond to the western (inner: $R \leq 2.^{\circ}5$; outer: $R > 2.^{\circ}5$) subregions, respectively.

best-fitting profile of the distribution of stars in the NE and SE outer subregions is a combination of two Gaussian functions, which are well separated (Fig. 4). The inner subregions are well fitted with a single Gaussian. The best-fitting parameters for $R \leq 3^{\circ}$ and $R > 3^{\circ}$ in the NE and SE are also shown in Table 1. The lower radial velocity component in the NE outer subregion is found to have a larger number of stars than the higher radial velocity component and the trend is opposite in the SE outer subregion. But note that the spectroscopic data used in our study could be incomplete and any comparison of the relative amplitudes of different components may not help to provide any reliable scientific insights. We performed the entire analysis with bin sizes of 5 and 15 km s^{-1} for the radial velocity distributions of all the subregions and found that a change in the bin size does not affect our final results. For further analysis and estimation of proper motions, we use the values based on the $R = 3^{\circ}$ cut for the NE and SE regions. Fig. 3 also shows two well-separated velocity components in the SW $R > 2.^{\circ}5$ outer region indicating the presence of a dual RGB population in the outer SW subregion as well.

The peak value of the higher velocity component of the NE ($R > 3^{\circ}$) and SE ($R > 3^{\circ}$) outer subregions is more similar/closer to the peak value of the single component in the respective inner regions. This suggests that the higher velocity component represents the radial velocity distribution of most of the stars in the SMC and hence could be the velocity distribution of stars in the main body of the SMC. The lower velocity component in the outer subregions might be the radial velocity distribution of the tidally affected stellar population. The differences in radial velocities between the two components are ∼35 and ∼45 km s^{-1} in the outer NE region ($R > 3^{\circ}$) and the outer SE ($R > 3^{\circ}$) subregions, respectively. However, in the SW ($R > 2.^{\circ}5$) outer subregion, the peak of the lower velocity component is similar to the peak of the single component in the inner SW subregion. This indicates the stars in the higher velocity component in the SW outer subregion could be associated with a substructure. The velocity difference between the two components in the outer SW region ($R > 2.^{\circ}5$) is ∼34 km s^{-1}. To better understand the connection between the different velocity components and the substructures, we compare their proper motion values with those of the RC stars.

3.2 Comparison of the proper motion values of the RGB and RC stars

To select the RGB stars corresponding to the single/double velocity components and analyse their proper motion properties in different subregions, we apply the following selection criterion. The stars that have velocities within the range peak velocity $-\sigma$ and peak velocity $+\sigma$ are selected and considered for further analysis. The peak velocity and the σ are the best-fitting values given in Table 1. In the outer NE, outer SE, and outer SW subregions, where dual RGB populations are found in the radial velocity distribution, the RGB stars in the lower and higher velocity components are separated using the respective peak velocity and σ values of the respective components. For these selected RGB stars in the different subregions, we estimated the median proper motion values in the RA and Dec directions. Before estimating the median values, we excluded stars having larger uncertainties (>0.1 mas yr^{-1}, which is two times the typical error associated with the proper motion values) in the proper motions. The median μ_{α} and μ_{δ} along with their standard errors for the inner and outer regions are tabulated in Table 2.

From Table 2, we can see that the proper motion values of the lower velocity component, especially in the NE outer and SE outer regions, are larger than the proper motion values of the higher velocity component. The obtained values of the two proper motion components of the lower and higher radial velocity components of RGB stars in the eastern subregions and their differences are comparable with the proper motion values of the foreground and main-body population of the RC stars in the $2.^{\circ}5$–$4.^{\circ}5$ radial range and their differences as given by Omkumar et al. (2021) (see their tables 3 and 4 and fig. 10) using *Gaia* DR2.

It will be interesting to make a comparison of the proper motions of the two radial velocity components of RGB stars with those of the two RC populations (foreground and main body) using the improved proper motion estimates from *Gaia* EDR3. Hence, we obtained the $5.^{\circ}0$ data of the SMC centred on the optical centre of the SMC by applying the same quality cuts used in Omkumar et al. (2021) from *Gaia* EDR3. We selected sources that are distributed in the same regions of the sky as in the studies of Dobbie et al. (2014) and De Leo et al. (2020) and merged them. The *Gaia* magnitudes (G, $G_{\rm BP}$, $G_{\rm RP}$) of the sources are corrected for interstellar extinction using the

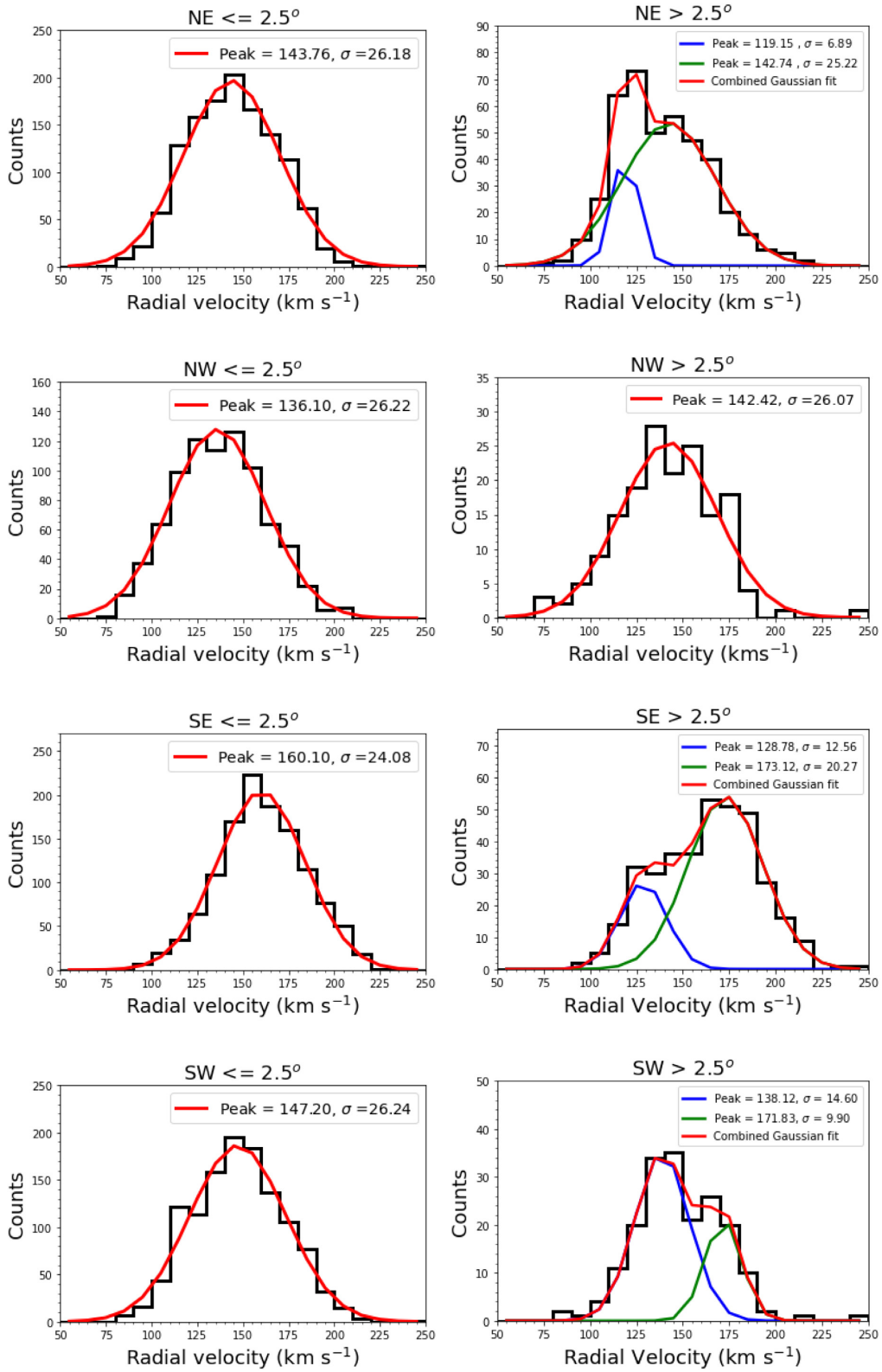

Figure 3. Radial velocity distributions (black line) along with their best-fitting Gaussian components are shown (blue and green lines) and the total fit is marked with a red line for the selected RGB sources in the NE (top row), NW (second row), SE (third row), and SW (bottom row) inner ($R \leq 2.^{\circ}5$; left-hand panel) and outer ($R > 2.^{\circ}5$; right-hand panel) subregions, respectively.

Table 1. Gaussian fit parameters for the radial velocity distributions of RGB stars.

Regions	Stellar counts	Lower velocity RGB		Higher velocity RGB	
		Peak 1 (km s^{-1})	Sigma 1 (km s^{-1})	Peak 2 (km s^{-1})	Sigma 2 (km s^{-1})
NE outer ($R > 2.^{\circ}5$)	413	119.15 ± 0.49	6.89 ± 3.76	142.74 ± 1.46	25.22 ± 6.76
NE inner ($R \leq 2.^{\circ}5$)	1262	–	–	143.76 ± 0.86	26.18 ± 6.72
NW inner ($R \leq 2.^{\circ}5$)	828	–	–	136.10 ± 0.70	26.22 ± 6.08
NW outer ($R > 2.^{\circ}5$)	166	–	–	142.42 ± 1.71	26.07 ± 9.43
SE outer ($R > 2.^{\circ}5$)	362	128.78 ± 1.92	12.56 ± 6.50	173.12 ± 1.40	20.27 ± 7.40
SE inner ($R \leq 2.^{\circ}5$)	1237	–	–	160.10 ± 0.69	24.08 ± 5.77
SW inner ($R \leq 2.^{\circ}5$)	1208	–	–	147.20 ± 1.02	26.24 ± 7.30
SW outer ($R > 2.^{\circ}5$)	188	138.12 ± 1.28	14.60 ± 5.90	171.83 ± 1.58	9.90 ± 5.14
NE outer ($R > 3^{\circ}$)	227	121.91 ± 1.65	12.41 ± 5.64	156.32 ± 3.22	14.56 ± 8.31
NE inner ($R \leq 3^{\circ}$)	1448	–	–	143.18 ± 1.14	26.23 ± 7.76
SE outer ($R > 3^{\circ}$)	148	131.42 ± 1.25	11.64 ± 5.27	176.87 ± 1.11	18.07 ± 6.54
SE inner ($R \leq 3^{\circ}$)	1451	–	–	160.74 ± 0.56	24.77 ± 5.28

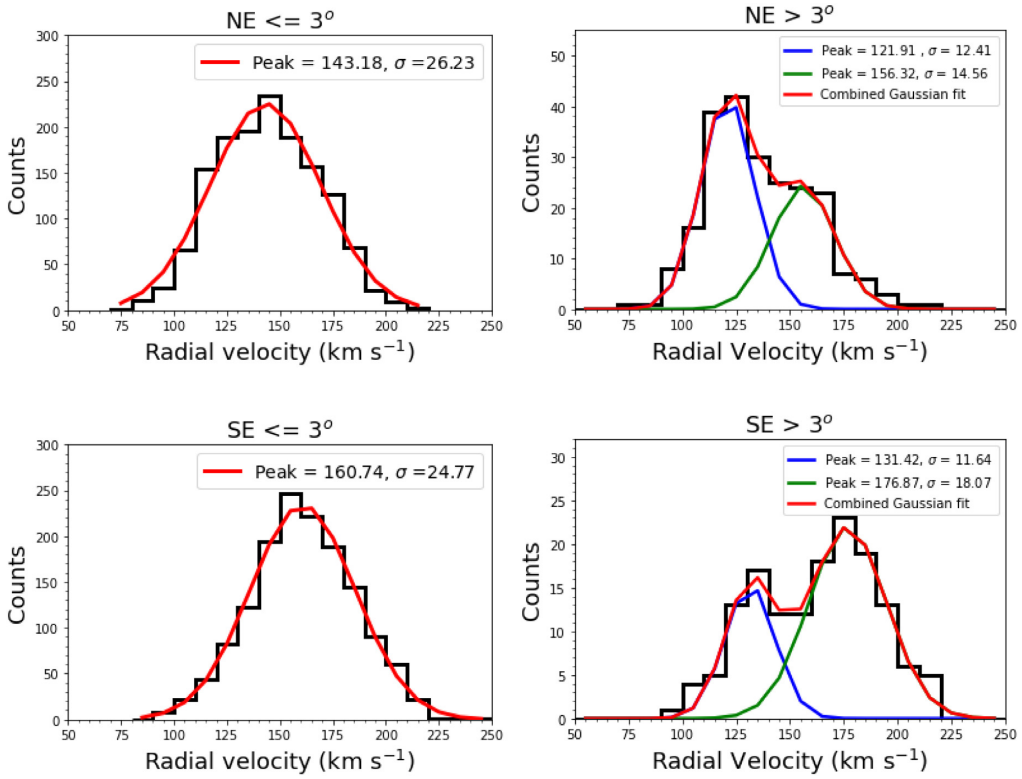

Figure 4. Radial velocity distributions (black line) with radial cut $R \leq 3^{\circ}$ and $R > 3^{\circ}$ along with their best-fitting Gaussian components in the NE outer (top right) and SE outer (bottom right) regions are shown. The total fit is marked as in Fig. 3 for the selected RGB sources.

Table 2. Median proper motion values of RGB and RC stars.

Regions	Lower velocity RGB		Higher velocity RGB		Foreground RC		Main-body RC	
	μ_α (mas yr^{-1})	μ_δ (mas yr^{-1})	μ_α (mas yr^{-1})	μ_δ (mas yr^{-1})	μ_α (mas yr^{-1})	μ_δ (mas yr^{-1})	μ_α (mas yr^{-1})	μ_δ (mas yr^{-1})
NE outer ($R > 3^{\circ}$)	1.088 ± 0.021	-1.250 ± 0.014	0.885 ± 0.029	-1.188 ± 0.017	1.092 ± 0.007	-1.241 ± 0.006	0.902 ± 0.007	-1.161 ± 0.006
NE inner ($R \leq 3^{\circ}$)	–	–	0.780 ± 0.007	-1.217 ± 0.008	–	–	0.795 ± 0.002	-1.167 ± 0.002
NW inner ($R \leq 2.^{\circ}5$)	–	–	0.623 ± 0.008	-1.262 ± 0.006	–	–	0.649 ± 0.003	-1.219 ± 0.002
NW outer ($R > 2.^{\circ}5$)	–	–	0.520 ± 0.017	-1.269 ± 0.018	–	–	0.532 ± 0.006	-1.230 ± 0.006
SE outer ($R > 3^{\circ}$)	1.156 ± 0.038	-1.327 ± 0.025	0.956 ± 0.027	-1.207 ± 0.022	1.101 ± 0.008	-1.296 ± 0.007	0.928 ± 0.008	-1.150 ± 0.007
SE inner ($R \leq 3^{\circ}$)	–	–	0.765 ± 0.007	-1.214 ± 0.007	–	–	0.768 ± 0.002	-1.172 ± 0.002
SW inner ($R \leq 2.^{\circ}5$)	–	–	0.585 ± 0.007	-1.232 ± 0.006	–	–	0.606 ± 0.002	-1.211 ± 0.002
SW outer ($R > 2.^{\circ}5$)	0.489 ± 0.029	-1.304 ± 0.023	0.460 ± 0.033	-1.257 ± 0.022	–	–	0.471 ± 0.005	-1.240 ± 0.004

extinction map (∼3° radial region of the SMC) provided by Rubele et al. (2018). For the stars in the region outside the coverage of their extinction map, we used the extinction values from the nearest region. We then divided the entire sample spatially to create similar subregions to those mentioned in Section 2.1 and selected RC stars from the G_0 versus $(G_{BP} - G_{RP})_0$ colour magnitude diagrams of the subregions. We produced the RC magnitude distributions in G_0 band with a bin size of 0.1 mag. The observed magnitude distributions of each subregion are initially fitted with a Gaussian function (for RC stars) and a quadratic polynomial (to account for RGB contamination in the RC selection) by using the curvefit function in PYTHON-SCIPY (Virtanen et al. 2020) and the best-fitting parameters (magnitudes and width along with their errors) are obtained. The fit to each of the subregions is repeated by adding an additional Gaussian component and further considered only if the χ^2 of the fit is improved by 25 per cent compared to a single Gaussian fit and the width of the second Gaussian is larger than the bin size of the distribution. Using this approach, we found that the NE and SE outer subregions have dual RC populations. The best-fitting parameters obtained for all the subregions are given in Table 3. As described in section 5 of Omkumar et al. (2021), we estimated the distances to each subregion. In the eastern outer subregions, where dual RC populations are found, we calculated the distances corresponding to the faint and bright RC populations (the faint RC corresponds to the main body of the SMC and the bright RC corresponds to a foreground population; refer to Table 3 for distance estimates). We then calculated the median proper motions (Table 2) of the selected RC stars in each subregion along with their respective uncertainties (which are standard errors associated with the median values) as described in section 6 of Omkumar et al. (2021). The estimated differences in the μ_α and μ_δ values of the two RC populations in the NE outer ($R > 3°$) subregion are $\sim 0.19 \pm 0.01$ and $\sim 0.08 \pm 0.01$ mas yr^{-1}, respectively. Similarly, the differences in the μ_α and μ_δ values in the SE outer ($R > 3°$) subregion are $\sim 0.17 \pm 0.01$ and $\sim 0.15 \pm 0.01$ mas yr^{-1}, respectively. We did not find any distance bimodality in the SW outer subregion in our analysis using RC stars.

Fig. 5 shows the median values of RGB stars in the lower and higher radial velocity components of the radial velocity distribution of the NE, SE, and SW outer subregions in the μ_α versus μ_δ plane. The median μ_α and μ_δ of the foreground and main-body RC populations (in the NE and SE) are also shown in the left-hand and middle panels of the plot for comparison. In the case of the SW outer subregion, as only a single RC component with distance similar to that of the main body is found, the median μ_α and μ_δ of the main-body RC is shown in the right-hand panel of the plot. The difference in the proper motion values between the two RGB populations is evident for the NE and SE outer subregions. Interestingly, in these subregions the proper motion values of RGB stars in the lower velocity component are very similar or comparable within errors to those of the foreground RC stars. This suggests that the RGB stars with lower velocities in the NE and SE outer subregions are part of the foreground substructure identified using RC stars. The proper motion values of RGB stars in the higher velocity component do not exactly match with those of the main-body RC population. The μ_α values are very similar, but the μ_δ values of RGB stars are larger than those of the RC stars. A similar difference in μ_δ values is observed between the single-velocity-component RGB and single-component RC in all other subregions (see Table 2). Since the discrepancy is only in one proper motion component, this rather points towards an intrinsic difference in velocity between the RGB and RC stars in the main body. If the RGB stars in the main body were at a closer distance than the RC stars in the main body, both proper motion components would be affected equally.

In the SW outer subregion, we compare the proper motion values from the higher and lower velocity RGB components with the proper motion value of the single-component RC (corresponding to the main-body distance) found in this region. The difference between the lower and higher velocity components is very small, with negligible difference in μ_α. The proper motion value of the higher velocity RGB component seems to be more similar to that of the main-body RC. However, as there is a negligible difference in the μ_α values of both the lower and higher velocity components and there seems to exist an intrinsic difference in the μ_δ values of the main-body RGB and RC, it is difficult to say whether the lower or the higher velocity RGB component is associated with the main body.

In the next subsection we compare the observed radial velocity and proper motion values of different RGB components with the values predicted for the SMC main body and the associated tidal features, from the *N*-body simulations (Diaz & Bekki 2012).

3.3 Comparison with simulations

The *N*-body simulations of the Magellanic System by Diaz & Bekki (2012) modelled the SMC as a multicomponent system consisting of a rotating disc, a non-rotating spheroid (the authors considered three models for the spheroidal component), and a dark matter halo and the LMC as a point mass. The SMC model with an extended spheroid (truncation radius = 7.5 kpc and scale length = 1.5 kpc) best reproduced the observed features. The Milky Way is modelled as a disc, bulge, and Navarro–Frenk–White (NFW) dark matter halo (Navarro, Frenk & White 1996). The panels of Fig. 6 show a comparison of the estimated proper motions (μ_α and μ_α in mas yr^{-1}) and radial velocities (km s^{-1}) of the lower velocity RGB component (black point) and higher velocity RGB component (red point) with the corresponding values from the simulated data points (for both the spheroidal and disc components separately) that are coloured according to distance for the NE, SE, and SW outer subregions. The observed median values of the proper motions and the peak of the radial velocity are taken from Tables 2 and 1, respectively. The distance to the centre of mass of the SMC used by Diaz & Bekki (2012) in the simulations is 61.6 kpc. As the mean distance to the main body of the SMC estimated from the RC stars by Omkumar et al. (2021) is 65.8 kpc and the proper motion values of the higher velocity RGB component are comparable to those of the main body of the RC, we considered the mean distance to the SMC as 65.8 kpc for the simulated points. This difference in the distance is applied as a systematic offset to the distance of the simulated data points and their proper motion values are also rescaled accordingly before comparing with the observed values. Most of the simulated data points are distributed at the main-body distance of the SMC. However, there are substructures at closer and farther distances from the main body. These substructures are suggested to be formed during the tidal interactions between the SMC and the LMC. The substructures are more prominent in the disc component. Diaz & Bekki (2012) suggested that the foreground substructure is part of the MB and the substructure at farther distance is referred to as the Counter-Bridge.

The plots (especially the comparison of the observed values with the predicted values for stars in the disc component) indicate that the two RGB components, separated in radial velocity and proper motion, are also separated by line-of-sight distance. In all the subregions shown, the lower radial velocity RGB component with higher proper motion values (shown as a black triangle) is at a shorter

Table 3. Magnitudes and distances of the RC stars in each subregion.

Subregions	Faint RC			Bright RC		
	Peak ± error	Width ± error	Distance ± error	Peak ± error	Width ± error	Distance ± error
NE outer ($R > 3°$)	18.932 ± 0.045	0.194 ± 0.031	66.375 ± 5.908	18.513 ± 0.046	0.145 ± 0.022	54.712 ± 3.639
NE inner ($R \leq 3°$)	18.778 ± 0.004	0.185 ± 0.004	61.808 ± 5.265	–	–	–
NW inner ($R \leq 2.^{\circ}5$)	18.781 ± 0.005	0.188 ± 0.006	61.913 ± 5.359	–	–	–
NW outer ($R > 2.^{\circ}5$)	18.987 ± 0.008	0.173 ± 0.007	68.054 ± 5.413	–	–	–
SE outer ($R > 3°$)	18.981 ± 0.019	0.164 ± 0.014	67.866 ± 5.113	18.512 ± 0.036	0.141 ± 0.023	54.701 ± 3.554
SE inner ($R \leq 3°$)	18.795 ± 0.005	0.185 ± 0.005	62.292 ± 5.305	–	–	–
SW inner ($R \leq 2.^{\circ}5$)	18.831 ± 0.005	0.195 ± 0.005	63.344 ± 5.668	–	–	–
SW outer ($R > 2.^{\circ}5$)	18.970 ± 0.009	0.172 ± 0.008	67.533 ± 5.344	–	–	–

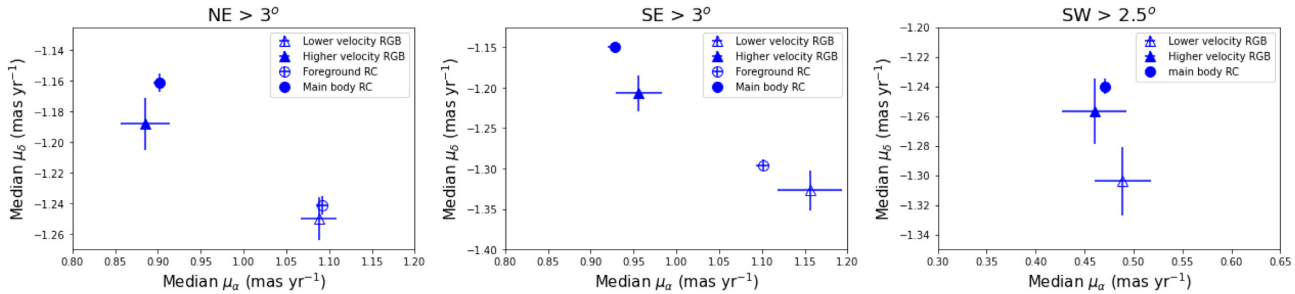

Figure 5. Observed median proper motions for lower velocity RGB sources (open triangle) and higher velocity RGB sources (filled triangle) in the NE outer ($R > 3°$), SE outer($R > 3°$), and SW outer ($R > 2.^{\circ}5$) subregions. Observed median proper motions for the foreground RC (open circle) and main-body RC (filled circle) are shown for comparison.

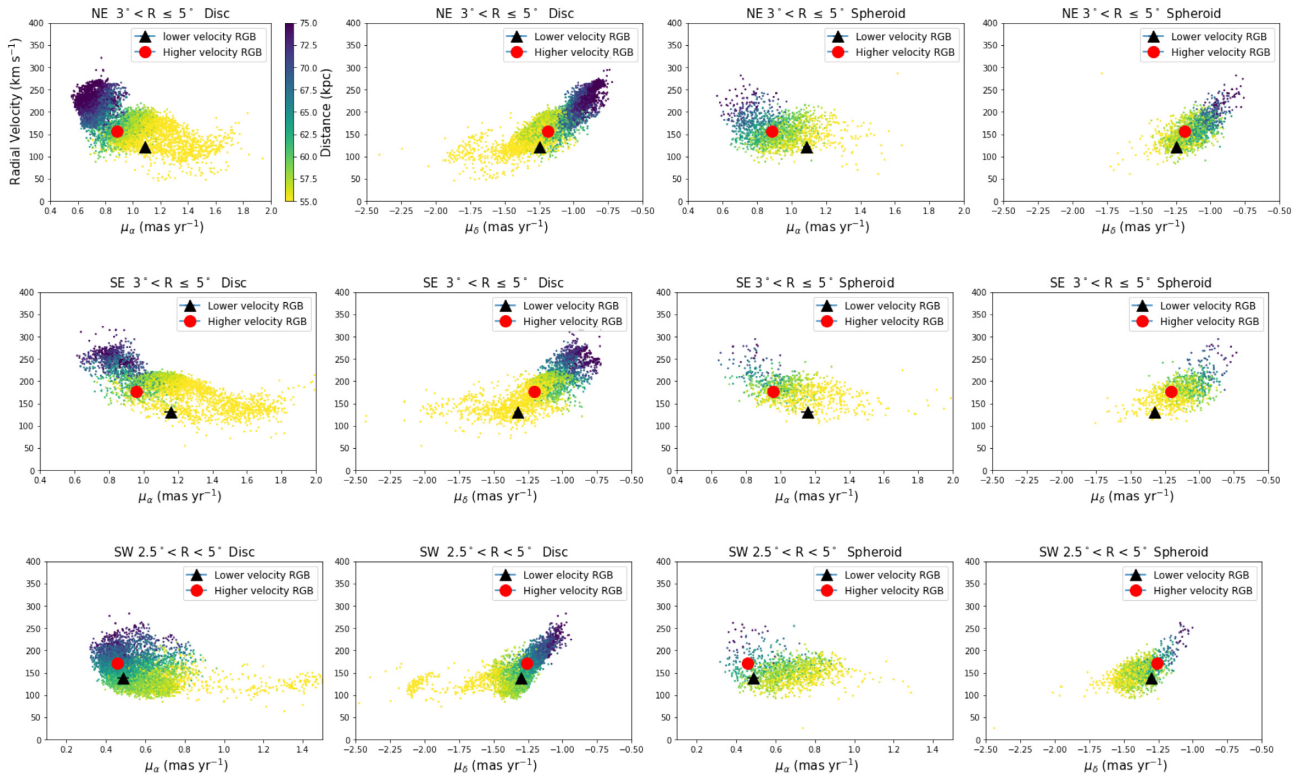

Figure 6. Radial velocity versus pmra and pmdec for the NE (top row), SE (middle row) 3.°0–5.°0 and SW (bottom row) 2.°5–5.°0 (outer) subregions. Simulated data points for the disc components and for the spheroid component of the SMC are shown with distance indicating the colour axis and the lower velocity RGB components and higher velocity RGB components are marked with black triangles and red circles, respectively.

line-of-sight distance compared to the higher radial velocity RGB component with lower proper motion values (shown as a red point). In the NE and SE outer subregions, the higher radial velocity RGB component is at the SMC main-body distance and the lower radial velocity RGB component is in the foreground of the main body. This is consistent with the results from the comparison of the proper motion values of the RC and RGB stars in Section 3.2. We did not find any signature of the presence of a Counter-Bridge in the NE and SE outer subregions from either the RGB or RC stars' analyses. The bottom panels of Fig. 6 suggest that in the SW outer subregion the lower radial velocity RGB component is at the main-body distance and the higher radial velocity RGB component is at a farther distance from the main body. This indicates the presence of RGB stars in the Counter-Bridge region of the SW SMC. As discussed in Section 3.2, we did not find any signature of the presence of the Counter-Bridge from the study of RC stars. The RC stars at the farther distance are expected to be fainter than the main-body RC stars and that might be the reason for the non-identification of this feature in *Gaia* data (where we expect the RC magnitudes in the Counter-Bridge to be close to the limiting magnitude). However, this feature was not identified either from the study of VMC data, where the RC magnitudes corresponding to the Counter-Bridge are expected to be ∼4–5 mag brighter than the limiting magnitude.

The comparison with the simulations suggests that the lower velocity RGB components identified in the NE and the SE outer subregions are at a closer distance to us than the main body of the SMC. Hence, they are part of the foreground substructure identified by the RC stars in earlier studies. Comparison with the simulations in the SW outer subregion indicates the presence of RGB stars in a substructure (Counter-Bridge) behind the main body of the SMC.

3.4 Epoch of formation of the RGB substructure

As RC stars are standard candles, Omkumar et al. (2021) calculated the distances of the foreground and main-body population of the RC stars in the SMC using *Gaia* DR2 data. Using data from *Gaia* EDR3 data and following the same analysis as Omkumar et al. (2021), we found that the foreground population of RC stars in the outer NE subregion is located at 11.67 ± 1.80 kpc in front of the main-body RC population of the SMC. We also estimated the distance differences between the dual population in the outer SE subregion as 13.17 ± 1.09 kpc. Since the lower and higher velocity components of the RGB stars have similar proper motion values to the foreground and main-body RC stars, we assume a similar distance separation between the two radial velocity components of the RGB stars. Also, the comparison with simulations suggests a similar distance separation between the RGB components. Using the relative velocities between the lower and higher velocity components in the NE (34.41 ± 3.62 km s^{-1}) and the SE (45.45 ± 1.67 km s^{-1}) and a distance separation of 11.67 ± 1.80 kpc in the NE and 13.17 ± 1.09 kpc in the SE between the two populations, we estimated the time of formation of this foreground stellar substructure as the difference in the distance divided by the difference in the radial velocity. We found the time-scale as 283 ± 25 and 331 ± 61 Myr based on the values from the NE and SE, respectively. Taking a mean of the two values, we see that the foreground stellar substructure was formed 307 ± 65 Myr ago. This time-scale is comparable with the recent direct collision/interaction between the MCs, predicted by simulations (Besla et al. 2012; Diaz & Bekki 2012), suggesting that the foreground stellar substructure might have formed in the most recent tidal interaction between the MCs.

This is a first-order calculation and we note that we have assumed the difference in distance and velocity only along the line of sight and there could be contributions from the components across the sky plane. As shown in Omkumar et al. (2021), the foreground RC substructure has ∼35 km s^{-1} slower tangential velocity than the main body of the SMC. Using that we can estimate the resultant velocity difference, but we do not have an independent estimate for the change in position of the substructure across the sky plane, which is essential to find the resultant distance difference. Another assumption in the calculation is that the the velocity difference between the main body and the foreground stellar substructure remains constant from the time of formation until today. If the substructure is currently accelerating, then the estimated time-scale is a lower limit, and if the substructure is currently decelerating, then the estimated time-scale is an upper limit.

4 SUMMARY

The eastern region of the SMC, in the direction of the Magellanic Bridge, is found to have a foreground stellar substructure, which is identified as a distance bimodality in the previous studies using RC stars. The RC stars in the substructure were also found to be kinematically distinct from RC stars in the main body of the SMC. This substructure was suggested to have been formed during the last tidal interaction between the Magellanic Clouds around 300 Myr ago, which formed the MB. If the substructure was formed in a tidal interaction, then different stellar populations older than 300 Myr are expected to be found in this substructure. However, RR Lyrae stars that are older than 10 Gyr are not found in this substructure, especially in the NE region of the SMC (see Muraveva et al. 2018; Tatton et al. 2020; Omkumar et al. 2021 for more details). Hence, it is essential to look for the presence/absence of other stellar populations in this foreground substructure to understand its nature and origin. Interestingly, RGB stars in the eastern region of the SMC show a bimodality in their radial velocity distribution. In this study, we investigate the connection between the bimodality in the radial velocity distribution of RGB stars and the bimodality in the distance distribution of RC stars, observed in the eastern regions of the SMC.

The two components in the radial velocity distribution of RGB stars are separated by ∼34 and ∼45 km s^{-1} in the NE and SE regions, respectively. Using archival spectroscopic data and *Gaia* EDR3 astrometric data of RGB stars, we found that the RGB stars with lower radial velocities have higher proper motion values than RGB stars with higher radial velocities. In these regions, the observed proper motion values of the RGB stars having lower and higher radial velocities are comparable with those of the foreground and main-body RC stars, respectively (separated by a line-of-sight distance of ∼11 and ∼13 kpc in the NE and SE regions, respectively). This suggests that the two RGB populations are separated by a line-of-sight distance of ∼11 and ∼13 kpc in the NE and SE regions, respectively, and the RGB stars with lower radial velocities are part of the foreground stellar substructure identified using RC stars. Comparison of the observed properties with *N*-body simulations also suggests that the RGB stars in the lower radial velocity component are at a shorter distance than the main-body population. Based on the differences in the distance and radial velocity values, we estimated the time of formation of the foreground substructure as 307 ± 65 Myr ago. This is comparable to the values predicted by simulations for the epoch of the most recent tidal interaction between the MCs. Our results provide evidence for the presence of another intermediate-age stellar population (RGB stars) in the foreground stellar substructure of the SMC, which was most likely formed during a tidal interaction about 307 ± 65 Myr ago.

We also identified a bimodal radial velocity distribution of RGB stars in the SW region of the SMC, where a distance bimodality

is not found in our analysis of RC stars. Comparison with the *N*-body simulations of the SMC indicates that the higher radial velocity component in the SW region is at a farther distance than the main body of the SMC. This indicates the presence of a counter-bridge, behind the main body of the SMC, in the SW region.

ACKNOWLEDGEMENTS

SS acknowledges support from the Science and Engineering Research Board of India through a Ramanujan Fellowship. AOO acknowledges support from the Indian Institute of Astrophysics for carrying out this research. MRC, FN, and AOO acknowledge support from the European Research Council (ERC) under the European Horizon 2020 research and innovation programme (grant agreement no. 682115). This research was supported in part by the Australian Research Council Centre of Excellence for All Sky Astrophysics in 3 Dimensions (ASTRO 3D), through project number CE170100013 (RdG). This work has made use of data from the European Space Agency (ESA) mission *Gaia* (https://www.cosmos.esa.int/gaia), processed by the *Gaia* Data Processing and Analysis Consortium (DPAC, https://www.cosmos.esa.int/web/gaia/dpac/consortium). Funding for the DPAC has been provided by national institutions, in particular the institutions participating in the *Gaia* Multilateral Agreement. In this work, we have used NUMPY (van der Walt, Colbert & Varoquaux 2011), SCIPY (Virtanen et al. 2020), MATPLOTLIB (Hunter 2007), and ASTROPY[1] (Astropy Collaboration 2013; Price-Whelan et al. 2018). Finally, it is our pleasure to thank the referee for an encouraging report.

DATA AVAILABILITY

The mean radial velocities and median proper motion values of RGB stars in different subregions are provided in various tables in the respective sections of the article. We used the radial velocity data of RGB stars in the SMC that were provided by Dobbie et al. (2014) and De Leo et al. (2020). The *Gaia* data used in the study were released as part of *Gaia* EDR3 and are available in the *Gaia* Archive at https://archives.esac.esa.int/gaia.

REFERENCES

Agertz O., Teyssier R., Moore B., 2011, MNRAS, 410, 1391
Astropy Collaboration, 2013, A&A, 558, A33
Bagheri G., Cioni M. R. L., Napiwotzki R., 2013, A&A, 551, A78
Belokurov V., Erkal D., Deason A. J., Koposov S. E., De Angeli F., Evans D. W., Fraternali F., Mackey D., 2017, MNRAS, 466, 4711
Besla G., Kallivayalil N., Hernquist L., van der Marel R. P., Cox T. J., Kereš D., 2012, MNRAS, 421, 2109
Carrera R., Conn B. C., Noël N. E. D., Read J. I., López Sánchez Á. R., 2017, MNRAS, 471, 4571
Chen C. H. R. et al., 2014, ApJ, 785, 162
Cioni M. R. L. et al., 2011, A&A, 527, A116
de Grijs R., Bono G., 2015, AJ, 149, 179
de Grijs R., Wicker J. E., Bono G., 2014, AJ, 147, 122
De Leo M., Carrera R., Noël N. E. D., Read J. I., Erkal D., Gallart C., 2020, MNRAS, 495, 98
de Vaucouleurs G., Freeman K. C., 1972, Vistas Astron., 14, 163
Demers S., Battinelli P., 1998, AJ, 115, 154
Diaz J. D., Bekki K., 2012, ApJ, 750, 36
Dobbie P. D., Cole A. A., Subramaniam A., Keller S., 2014, MNRAS, 442, 1663
El Youssoufi D., 2019, in A Synoptic View of the Magellanic Clouds: VMC, Gaia and Beyond. Leibniz Institute of Astrophysics Potsdam (AIP), Potsdam, Germany, p. 51
El Youssoufi D. et al., 2021, MNRAS, 505, 2020
Fall S. M., Efstathiou G., 1980, MNRAS, 193, 189
Gaia Collaboration, 2016, A&A, 595, A2
Gaia Collaboration, 2018, A&A, 616, A1
Gaia Collaboration, Brown A. G. A., Vallenari A., Prusti T., de Bruijne J. H. J., Babusiaux C., Biermann M., 2021, A&A, 649, A1
Groenewegen M. A. T. et al., 2019, A&A, 622, A63
Hammer F., Yang Y. B., Flores H., Puech M., Fouquet S., 2015, ApJ, 813, 110
Harris J., 2007, ApJ, 658, 345
Hunter J. D., 2007, Comput. Sci. Eng., 9, 90
Jacyszyn-Dobrzeniecka A. M. et al., 2017, Acta Astron., 67, 1
Jacyszyn-Dobrzeniecka A. M. et al., 2020, ApJ, 889, 26
Kallivayalil N., van der Marel R. P., Alcock C., Axelrod T., Cook K. H., Drake A. J., Geha M., 2006, ApJ, 638, 772
McMahon R. G., Banerji M., Gonzalez E., Koposov S. E., Bejar V. J., Lodieu N., Rebolo R., VHS Collaboration, 2017, The Messenger, Vol. 154. p.35
Massana P. et al., 2020, MNRAS, 498, 1034
Muraveva T., Delgado H. E., Clementini G., Sarro L. M., Garofalo A., 2018, MNRAS, 481, 1195
Navarro J. F., Frenk C. S., White S. D. M., 1996, ApJ, 462, 563
Nidever D. L., Majewski S. R., Butler Burton W., 2008, ApJ, 679, 432
Nidever D. L., Majewski S. R., Muñoz R. R., Beaton R. L., Patterson R. J., Kunkel W. E., 2011, ApJ, 733, L10
Nidever D. L., Monachesi A., Bell E. F., Majewski S. R., Muñoz R. R., Beaton R. L., 2013, ApJ, 779, 145
Nidever D. L. et al., 2019, ApJ, 887, 115
Noël N. E. D., Conn B. C., Carrera R., Read J. I., Rix H. W., Dolphin A., 2013, ApJ, 768, 109
Noël N. E. D., Conn B. C., Read J. I., Carrera R., Dolphin A., Rix H. W., 2015, MNRAS, 452, 4222
Omkumar A. O. et al., 2021, MNRAS, 500, 2757
Price-Whelan A. M. et al., 2018, AJ, 156, 123
Price-Whelan A. M., Nidever D. L., Choi Y., Schlafly E. F., Morton T., Koposov S. E., Belokurov V., 2019, ApJ, 887, 19
Putman M. E., Staveley-Smith L., Freeman K. C., Gibson B. K., Barnes D. G., 2003, ApJ, 586, 170
Ramachandran V., Oskinova L. M., Hamann W. R., 2021, A&A, 646, A16
Richter P. et al., 2017, A&A, 607, A48
Rubele S. et al., 2018, MNRAS, 478, 5017
Salem M., Besla G., Bryan G., Putman M., van der Marel R. P., Tonnesen S., 2015, ApJ, 815, 77
Schmidt T., Cioni M.-R., Niederhofer F., Diaz J., Matijevic G., 2019, in McQuinn K. B. W., Stierwalt S., eds, Proc. IAU Symp., Vol. 344, Dwarf Galaxies: From the Deep Universe to the Present. Kluwer, Dordrecht, p. 130
Skowron D. M. et al., 2014, ApJ, 795, 108
Subramanian S. et al., 2017, MNRAS, 467, 2980
Tatton B. L. et al., 2020, MNRAS, 504, 2983
Tepper-García T., Bland-Hawthorn J., Pawlowski M. S., Fritz T. K., 2019, MNRAS, 488, 918
van den Bosch F. C., 2002, MNRAS, 331, 98
van der Marel R. P., Cioni M.-R. L., 2001, AJ, 122, 1807
van der Walt S., Colbert S. C., Varoquaux G., 2011, Comput. Sci. Eng., 13, 22
Vieira K. et al., 2010, AJ, 140, 1934
Virtanen P. et al., 2020, Nat. Methods, 17, 261
Wagner-Kaiser R., Sarajedini A., 2017, MNRAS, 466, 4138
Wang J., Hammer F., Yang Y., Ripepi V., Cioni M.-R. L., Puech M., Flores H., 2019, MNRAS, 486, 5907
Zivick P. et al., 2018, ApJ, 864, 55
Zivick P. et al., 2019, ApJ, 874, 78

[1] http://www.astropy.org

This paper has been typeset from a TEX/LATEX file prepared by the author.